Indications of surface-dominated transport in single crystalline nanoflake devices of topological insulator $Bi_{1.5}Sb_{0.5}Te_{1.8}Se_{1.2}$

Bin Xia,[1,*] Peng Ren,[1,*] Azat Sulaev,[1] Peng Liu,[1] Shun-Qing Shen,[2] and Lan Wang[1,†]

[1]*School of Physical and Mathematical Science, Nanyang Technological University, Singapore, 637371, Singapore*

[2]*Department of Physics, The University of Hong Kong, Pokfulam Road, Hong Kong, People's Republic of China*

(Received 13 March 2012; revised manuscript received 19 December 2012; published 27 February 2013)

We report experimental evidence of surface-dominated transport in single crystalline nanoflake devices of topological insulator $Bi_{1.5}Sb_{0.5}Te_{1.8}Se_{1.2}$ (BSTS). The resistivity measurements show dramatic differences between the nanoflake devices and bulk single crystal. Based on a two-channel model, the analysis on the resistivity and Hall resistance indicates that ∼99% surface transport contribution can be realized in 200 nm-thick BSTS nanoflake devices. Using a standard back gate with SiO_2 as a dielectric layer, a pronounced ambipolar electric field effect was observed in devices fabricated with 100–200 nm thick flakes. Moreover, angle-dependent magnetoresistances of a nanoflake device with a thickness of 596 nanometers are fitted to a universal curve for the perpendicular component of the applied magnetic field. The value of phase coherence length obtained from two-dimensional weak antilocalization fitting further confirmed the surface dominated transport. Our results open a path for realization of electric and spintronic devices based on the topological helical surface states.

DOI: 10.1103/PhysRevB.87.085442 PACS number(s): 73.25.+i, 72.20.My, 73.20.Fz, 73.23.−b

I. INTRODUCTION

Topological insulators (TIs) are gapped bulk insulators with gapless Dirac surface states.[1–4] The surface states of these topological insulators are spin polarized and protected by time-reversal symmetry. A number of surface spectroscopy measurements, such as spin and angle-resolved photoemission spectroscopy (ARPES)[5–13] and scanning tunneling microscopy,[14,15] have been used to detect the topologically nontrivial surface state in three-dimensional (3D) topological insulator $Bi_{1-x}Sb_x$, Bi_2Se_3, Bi_2Te_3, etc. The exotic surface states of topological insulators are expected to form a playground of various topological quantum effects and show great potential in spintronics and quantum computation.[16–18] To fulfill the expectations, realizing topological insulator systems with significant surface transport is essential. However, due to the defects or impurities in the samples, it is extremely difficult to eliminate the bulk contribution to electron transport.[19–24] Realizing surface-dominated transport in current topological insulator systems is still a challenge despite extensive efforts involving chemical doping,[22,33–39] thin film or nanostructure fabricating,[25–32] and electrical gating. [21,26,32,43]

In this paper, we present strong evidence for surface-dominated transport in nanoflake devices fabricated with topological insulator $Bi_{1.5}Sb_{0.5}Te_{1.8}Se_{1.2}$ (BSTS) flakes with a thickness of several hundred nanometers. We performed electron transport measurements of both bulk single crystals and nanoflake devices of high-quality single crystalline BSTS. Nanoflake devices show a transition from semiconductor to metal near 100–150 K with decreasing temperature, while bulk crystals shows semiconductor behavior in the measured temperature range from 300 K to 10 K and only present resistance saturation at very low temperature (<40 K). At 10 K, the resistivity of the nanoflake devices decreases with the sample thickness and can get to hundreds of times smaller than that of the bulk single crystal. Back-gated devices fabricated with 150–200 nm thick BSTS nanoflakes show pronounced ambipolar electric field effect, which demonstrates significant topological surface transport. It was also found that the angle-dependent magnetoresistances of a 596-nanometer thick nanoflake devices are fitted to a universal curve for the perpendicular component of an applied magnetic field. The phase coherence length obtained from a two-dimensional weak antilocalization fitting is much smaller than the sample thickness (596 nm), which clearly proves the 2D surface transport in the device. All the experimental results suggest that surface dominated transport has been realized in BSTS devices with a thickness of several hundreds of nanometers.

II. EXPERIMENT

High-quality BSTS single crystals were grown using modified Bridgeman methods. High-purity (99.9999%) Bi, Sb, Te, and Se with a molar ratio of 1.5:0.5:1.8:1.2 were first thoroughly mixed and then reacted at 950°C for one week in an evacuated quartz tube in a box furnace. We then located the quartz tube vertically in a specially designed furnace with large temperature gradient. The temperature is then decreased to room temperature over three weeks, with different cooling speed in different temperature regions. The obtained crystals are easily cleaved and revealed a flat and big shiny surface as shown in the inset of Fig. 1(a). An as grown single crystal is a cylinder with ∼0.7 cm^2 (the cross section area) × 2 cm (height). Large cleaved crystals can be cut from different positions of the crystal.

The x-ray diffraction pattern indicates the high quality of our samples. Figure 1(a) shows the wide angle x-ray diffraction from a bulk crystal oriented with the scattering vector perpendicular to the (001) family of planes. No peaks from other plane families can be observed. It should be noted that the count of the (006) peak is larger than 300 k. Only high-quality single crystals can get to this value in XRD facility. The inset of Fig. 1(a) shows the large and shining (001) surface of the single crystal. Energy dispersive x-ray spectroscopy (EDS) was employed to probe the homogeneity of the samples. The small area EDS mapping as shown in Fig. 1(b) indicates that

 ©2013 American Physical Society

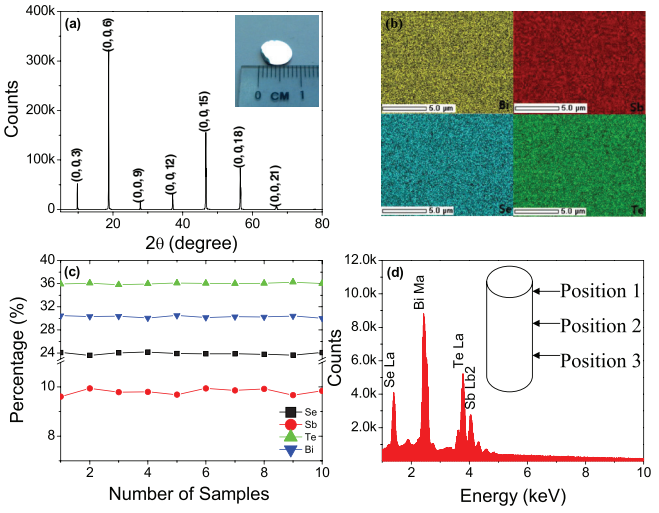

FIG. 1. (Color online) Summary of structural characterization. (a) Shows the wide angle x-ray diffraction from a bulk crystal oriented with the scattering vector perpendicular to the (100) family of planes. Inset is a photograph of a typical crystal. (b) The EDS mapping of a small area in a BSTS single crystal. (c) Molar ratio of Bi, Sb, Te, and Se at ten random positions in a big crystal like the one shown in the inset of (a). (d) A typical EDS spectroscopy. The inset is a schematic diagram of an as-grown single crystal.

the element distribution in a small area is homogeneous. We also performed the EDS measurements at various points of the bulk single crystal used in our measurements. As shown in Fig. 1(c), the molar ratio of the four elements at various points of the big crystal only shows small fluctuations in the ~8 mm × 8 mm single crystal, which means a large crystal cut from one position [the meaning of position is shown in the inset of Fig. 1(d)] is quite homogeneous. Small crystals cut from this 8 mm × 8 mm big crystal show very similar transport behaviors.

The molar ratio of (Bi + Sb)/(Se + Te) and Bi/Sb in crystals cut from different positions of the crystal cylinder shows near-constant molar ratios of 2/3 and 3/1, respectively, while the Te/Se ratio changes from ~1.7/1.3 to ~1.9/1.1 for crystals obtained from different positions. Transport measurements show that, although the molar ratio of Te/Se varies with position as shown in the inset of Fig. 1(d), all the crystals show similar semiconducting ρ (T) curve at high temperature and saturation behavior at low temperature and large resistivity (>1 Ω cm) at 10 K. The value of ρ(10 K)/ρ(300 K) can vary from 30 to 250. This characteristic of BSTS is very different from the condition of grown Bi_2Te_3 single crystals. Bi_2Te_3 single crystals obtained from different part of the cylinder usually show different transport behaviors, from metallic to semiconducting. We choose BSTS crystals with ρ(10 K)/ρ(300 K) > 100 and ρ(10 K) > 3 Ω cm for our experiments.

For the transport measurements on bulk samples, the contact were made with silver paste and cured at room temperature. Photolithography was used to pattern electrodes on the nanoflake devices. Cr/Au (5 nm/120 nm) contacts were deposited in a magnetron sputtering system with a base pressure of 1×10^{-8} torr. The typical devices are shown in Figs. 2(g) and 2(h). Standard lock-in technique was employed to perform four-terminal magnetoresistance and Hall measurements in a 9 Tesla Quantum Design PPMS system. All the transport measurements were performed with the applied current in the (001) plane.

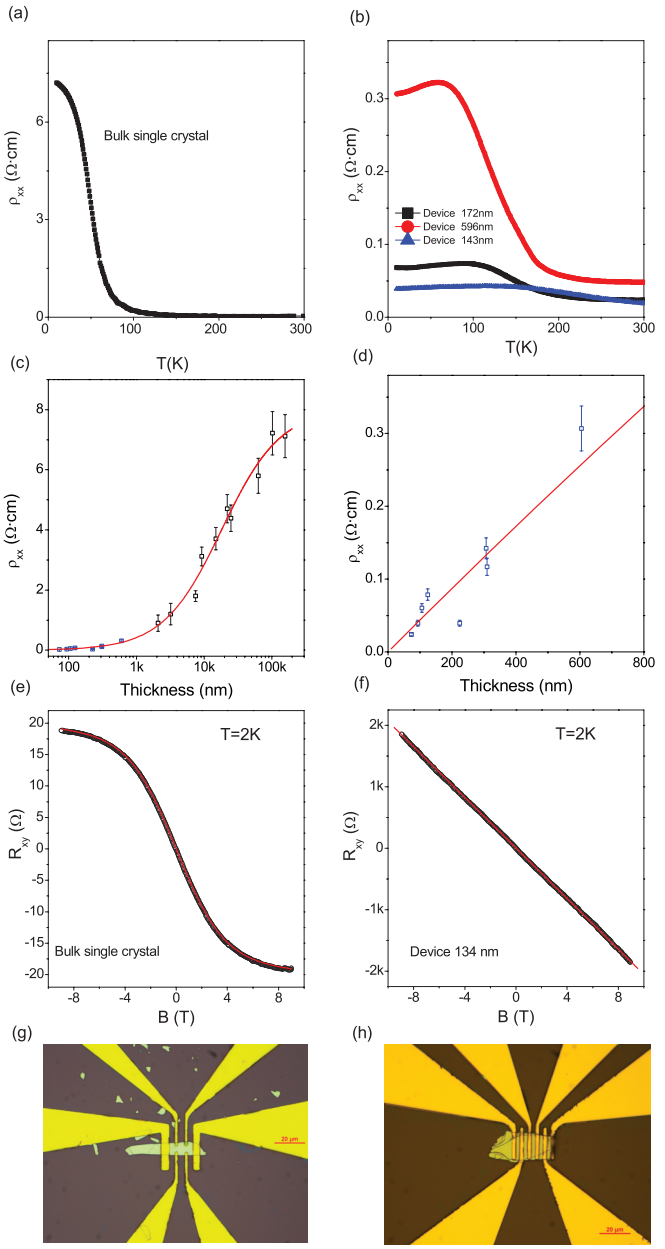

FIG. 2. (Color online) Temperature dependence of resistivity in zero field of (a) bulk single crystal with a thickness of 102 μm and (b) nanoflake devices with various thicknesses. (c) The resistivity values of nanoflake devices and bulk crystals with various thicknesses. The red line is the fitting curve based on the two-channel model. (d) The zoom in of Fig. 2(c). It shows the thickness of the resistivity of nanoflake devices. (e) The Hall measurement results of the 102-μm thick BSTS single crystal and the fitting (the red curve) based on a two-channel model. (f) The Hall resistance of a BSTS nanoflake device with a thickness of 134 nm. The red line is a drawn straight for comparison. (g) and (h) The image of two typical devices for transport measurements.

III. RESISTIVITY, HALL RESISTANCE, AND AMBIPOLAR ELECTRIC GATING EFFECT

The temperature dependence of the resistivity of the bulk single crystal and three nanoflake devices measured in zero field are shown in Figs. 2(a) and 2(b), respectively. The 102-μm thick bulk crystal shows semiconductor behavior in the measured temperature regime and reaches a saturation behavior when $T < 40$ K, which is due to the increasing transport contribution from surface.[37,38] The resistivity at 10 K is more than 200 times larger than that at room temperature. Although the nanoflake devices also show the semiconductor behavior in the high-temperature range, the transport characteristics transfer to a metallic type when $T < 150$ K. It should be noted from Figs. 2(a) and 2(b) that the resistivity of nanoflakes are hundreds of times smaller than that of the bulk single crystal although the nanoflake is exfoliated from the bulk crystal used in the transport measurement [Fig. 2(a)]. As shown in the inset of Fig. 2(b), the resistivity of eight nanoflake devices with varying thickness smaller than 600 nm and the nine bulk single crystals with thickness between 1 μm to 157 μm at 10 K decreases with decreasing sample thickness. The eight nanoflake devices and 102-μm thick bulk sample are obtained from the same piece of single crystal, while the other eight bulk samples are obtained from another piece of single crystal. From the systematic decrease of resistivity with decreasing sample thickness and the energy-dispersive x-ray spectroscopy (EDS) as shown in Fig. 1, we can conclude that the dramatic decrease of resistivity with decreasing sample thickness is not due to chemical inhomogeneity. As the material system has already been proved to be a topological insulator,[36,37] the dramatic decrease of resistivity with decreasing sample thickness indicates that the contribution from the surface states plays a more and more important role as the thickness reduces. As shown in Fig. 3, supposing that the total thickness of the two surface states is 5 nm, we use a simple model to fit the resistivity of the surface states and bulk. The formulas are shown below,

$$R = \frac{1}{\frac{1}{R_b} + \frac{1}{R_s}} = \frac{1}{\frac{w \cdot t_b}{\rho_b \cdot l} + \frac{w \cdot t_s}{\rho_s \cdot l}} = \frac{\rho_s \cdot \rho_b \cdot l}{(t_s \cdot \rho_b + t_b \cdot \rho_s) \cdot w} \quad (1)$$

$$\rho = \frac{\rho_b \rho_s (t_b + t_s)}{t_s \rho_b + t_b \rho_s}, \quad (2)$$

where ρ, ρ_b, ρ_s, t_b, t_s, are the resistivity of the sample, the resistivity of the bulk part, the resistivity of a 5 nm thick surface state, the thickness of the bulk, and the thickness of the surface state (5 nm), respectively. The fitting curve is shown as the red line in the inset of Fig. 2(c), which yields $\rho_b = 8.036\ \Omega$ cm and $\rho_s = 2.19 \times 10^{-3}\ \Omega$ cm. For a device with a thickness of 200 nanometers, the conductance contribution of the surface states is 98.9% at 10 K. Figure 2(d) is the zoom in of Fig. 2(c), which shows the resistivity of the eight nanoflake devices more clearly. As shown in Fig. 2(e), the Hall measurement of the single crystal (102 μm) is also fitted using a standard two-band model [32,38] (details in Appendix),

$$\rho_{xy}(B) = -\frac{B}{e} \frac{(n_b \mu_b^2 + n_s \mu_s^2 / t) + B^2 \mu_b^2 \mu_s^2 (n_b + n_s / t)}{(n_b \mu_b + n_s \mu_s / t)^2 + B^2 \mu_b^2 \mu_s^2 (n_b + n_s / t) 2}, \quad (3)$$

where ρ_{xy}, B, n_b, n_s, μ_b, μ_s, and t are the Hall resistivity, magnetic field, bulk charge density, surface charge density, bulk mobility, surface mobility, and sample thickness, respectively. The fitting yields $n_b = 1.1 \times 10^{17}$ cm^3, $n_s = 2.5 \times 10^{12}$ cm^2, $\mu_b = 25$ cm^2/V s, $\mu_s = 1767$ cm^2/V s. Based on the fitting results, the surface conductance contribution of a 200-nm thickness sample is 98.7%, which agrees well with the results obtained from resistance measurements. It should be noted that the results obtained from the fitting of Hall resistivity has certain arbitrariness due to the multiple free parameters. To relieve the arbitrariness and further prove the surface dominated transport in nanoflakes with a thickness of hundred nanometers, we measured the Hall resistance of a nanoflake device (134-nm thick) from 9 T to -9 T. As shown in Fig. 2(f), the shape of Hall resistance vs magnetic field curve is very different from that of the bulk sample in Fig. 2(e). The Hall resistance of the nanoflake is always linear over the entire range of magnetic field, indicating all channels contributing to the transport have similar mobility and the same carrier sign. The transport channels of nanoflake devices include the top and bottom surfaces, the side surfaces, and the bulk channel. As it is known that the mobility of the bulk channel of BSTS is much smaller than that of the surface transport channels, from the perfect linear behavior of the Hall resistance, it can be concluded that the bulk transport is negligible in the nanoflake device at 2 K. Otherwise, the Hall resistance vs magnetic field curve will show clear curvature due to the transport channels with very different mobility. The linear Hall resistance also shows that the mobility of electrons on the top, side, and bottom surface are similar, which indicates that the device fabrication process does not significantly change the mobility of the top and side surfaces of BSTS samples. The Hall resistance of the nanoflake device is 207 Ω/T, which corresponds to a Hall carrier density of 3.01×10^{12} cm^{-2}. The sheet resistance of the device at 2 K is 1260 Ω, therefore the mobility of the surface transport can be calculated as 1647 cm^2/V s. Both the charge density and mobility of the surface state obtained from the direct measurements agrees well with the value obtained by the fitting on the bulk Hall measurements [Fig. 2(e)], which further support the ~99% surface transport in a BSTS device with a thickness of 200 nm.

If the electron transport is mainly due to the topological surface transport, we should be able to observe the ambipolar electric effect even in devices fabricated with BSTS nanoflakes with a thickness of several hundred nanometers, which is

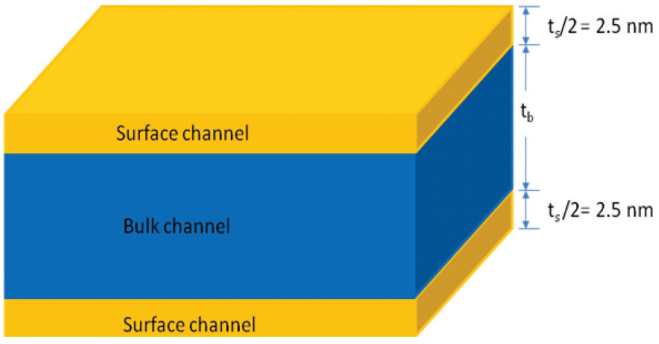

FIG. 3. (Color online) Schematic diagram of a two-channel model for resistivity of BSTS nanoflake device.

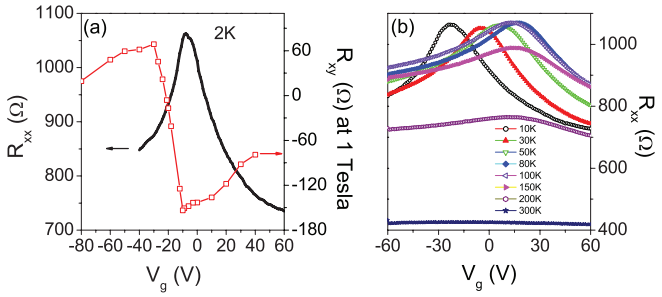

FIG. 4. (Color online) (a) The gate voltage dependence of resistance (R_{xx}) and Hall resistance (R_{xy}) at 1 Tesla field of a BSTS nanoflake device at 2 K. (b) The temperature evolution of the $R_{xx}(V_g)$ curve.

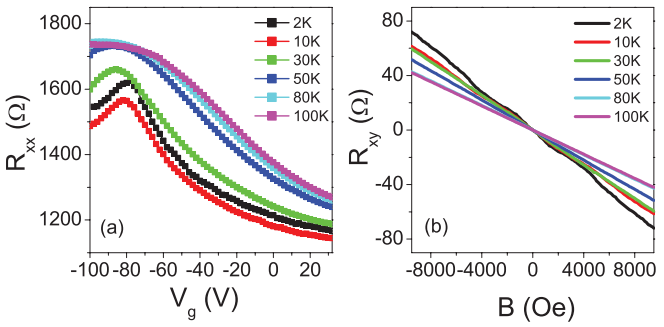

FIG. 5. (Color online) (a) The $R_{xx}(V_g)$ curves of a BSTS nanoflake devices at various temperatures. The devices had been stored in vacuum for two months. The peak shifts to -80 volts. (b) The low field Hall resistance of the device.

indeed the case in our experiments. Figure 4 shows the gate-voltage dependence of longitudinal resistance (R_{xx}) without applied magnetic field and Hall resistance (R_{xy}) at 1 Tesla magnetic field of a 172-nm thick device. To eliminate any possible nonsymmetry effect of the sample and electrode contacts, all the Hall resistances were obtained from low field Hall measurement with magnetic field scanning from -1 Tesla to 1 Tesla. As the sample is 172-nm thick, the electrostatic gating can only shift the Fermi level of the bottom surface. The key finding is the resistance maxima appears near $V_g = -10$ V. The resistance change near 35% with ±60V applied gate voltage. The quite sharp charge neutrality point at 2 K and the gradual decrease of resistance with V_g deviating from the charge neutrality point indicate that the ambipolar behavior should be due to the Dirac cone of the topological surface state, which has been observed by ARPES.[36] If it were due to the normal band banding, there would be a wide constant resistance region when the Fermi level is in the band gap and a much dramatic resistance decrease when the Fermi level enters into conduction or valence band. The Hall resistance can also be changed from n type to p type with applied gate voltage as shown in Fig. 4(a), which further confirms the ambipolar electric gating effect in this device. From the measured Hall resistance R_H (150 Ω/T at 2 K), if we neglect the Hall contribution from the bulk, the charge density can be estimated to be about 4.2×10^{12} cm^{-2} (bottom + top), which approximately agrees with the bulk Hall fitting results as aforementioned. For a 300-nm SiO_2 dielectric layer, a gate voltage of 60 volts can induces $n = 4.4 \times 10^{12}$ cm^{-2}, therefore the 300 nm SiO_2 dielectric layer should be able to generate ~50% resistance change because we can only tune the bottom surface state. However, considering the 176-nm thick side surface of the devices, which can contribute ~5–10% surface conductance contribution, and the small amount of charge from the bulk, it is very reasonable that we only get 30–40% resistance change. It should be pointed out that we have observed similar ambipolar behavior in many devices fabricated with BSTS flakes with a thickness of several hundred nm. Figure 4(b) shows the gate voltage dependence of resistance at various temperatures. It is observed that the shape of the $R(V_g)$ curves become more broad with increasing temperature, which is a standard ambipolar behavior as shown in graphene.[40] It also agrees well with the deceasing surface conductance contribution with increasing temperature. The shift of resistance peaks with increasing temperature indicates the shift of chemical potential of the bottom surface with increasing temperature. The ambipolar gating effect of a device stored in vacuum for two months is shown in Fig. 5, which indicates that the charge neutrality point shifts to near -80 V.

IV. WEAK ANTILOCALIZATION

To further confirm the surface-dominated electron transport in the nanoflake device, we have performed the angle-dependent magnetoresistance measurements using a very thick (596 nm) nanoflake device. To eliminate any effect from Hall resistance, all the magnetoresistance measurements were performed from -2 Tesla to 2 Tesla and carried out corresponding calculation process to obtain intrinsic magnetoresistance. The magnetoresistance was measured by tilting the bulk crystal and nanoflake device with respect to the applied magnetic field from 0° to 90°. $\theta = 0°$ means the magnetic field parallel to the (001) surface while the $\theta = 90°$ means the magnetic field perpendicular to the (001) surface. Figures 6(a)–6(d) show the field dependence of magnetoconductances $\Delta G = G(B) - G(0)$ with various θ for the bulk single crystal at 2 K and nanoflake device at 2 K, 10 K, and 30 K, respectively. Both the bulk crystal and nanodevice show weak antilocalization behavior in the low magnetic field region. Such a weak antilocalization at low temperature has been attributed to both strong spin-orbital coupling and topological π Berry phase of two-dimensional surface states.[41,46] It is very obvious that ΔG decreases with decreasing θ for both bulk single crystal and nanoflake device and it is more pronounced for the nanoflake device. The variation of magnetoconductance as a function of the perpendicular component of the magnetic field for the bulk single crystal at 2 K and nanoflake device at 2 K, 10 K, and 30 K are shown in Figs. 6(e)–6(h), respectively. The G vs $B \sin\theta$ (the perpendicular component of the applied field) curves of the nanoflake device are perfectly merged into one universal curve at all temperatures. It should be noticed that a misalignment between the sample and applied magnetic field has a large effect when θ is near 0 while it has a negligible effect when θ is a large value, which can be inferred from the small difference between the $\theta = 80°$ and $\theta = 90°$ curves and the large difference between

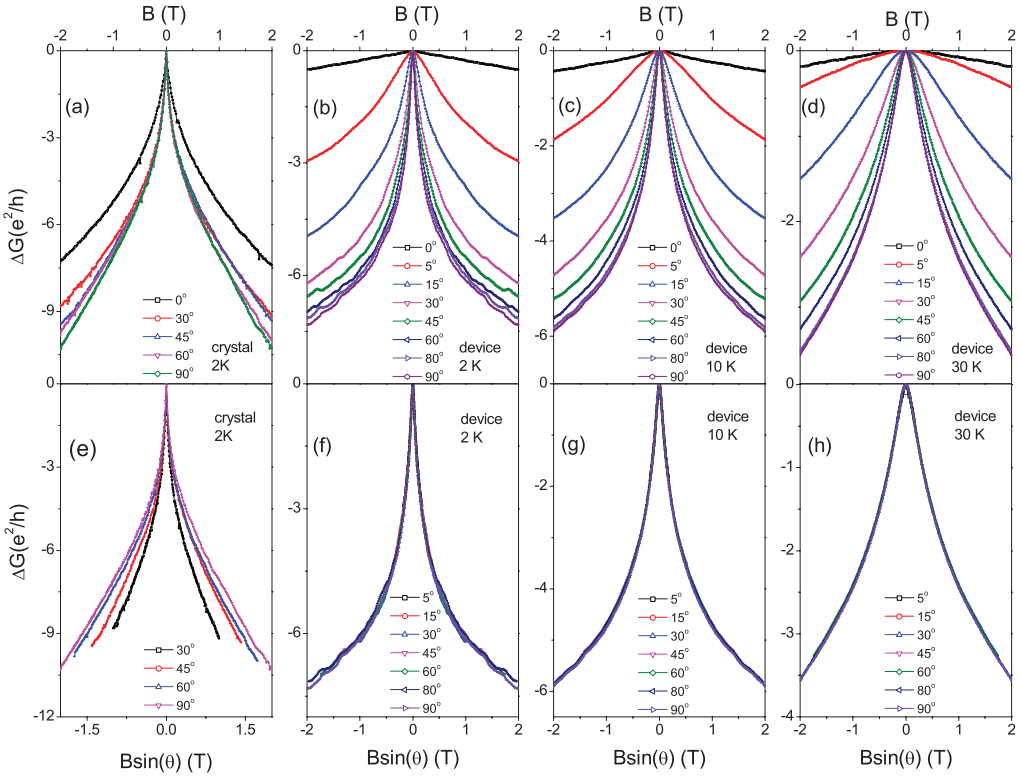

FIG. 6. (Color online) Angle-dependent conductance of a bulk BSTS single crystal and a nanodevice fabricated with a 596-nm thick BSTS flake. θ is the angle between the direction of the magnetic field and the (001) plane. (a), (b), (c), and (d) show the magnetoconductance of bulk BSTS single crystal at 2 K, nanoflake device at 2 K, 10 K, and 30 K, respectively. (e), (f), (g), and (h) show the curves of magnetoconductance vs the perpendicular component of the magnetic field of bulk BSTS single crystal at 2 K, nanoflake device at 2 K, 10 K, and 30 K, respectively.

$\theta = 0^\circ$ and $\theta = 5^\circ$ curves. Based on this, we speculate that the very small magnetoconductance at $\theta = 0^\circ$ may be due to the small unavoidable misalignment between the sample and the applied magnetic field in experiment. Therefore, the perfect fitting into a universal curve for all θ value (except $\theta = 0^\circ$) as shown in Figs. 6(f)–6(h) is a support of the conclusion obtained from the resistivity and Hall measurements, surface-dominated transport (96.9% in a 596-nm thick device). For the bulk single crystal, it is not a surprise that the weak antilocalization is observed for all the angles and G vs $B \sin\theta$ curve cannot be fitted to one universal curve because of the coexistence of both the bulk spin-orbit coupling effects and helical surface state contribution.

Magnetoconductances ΔGat different temperatures (2 K, 4 K, 7 K, 10 K, 15 K, 30 K, and 45 K) have been obtained in a magnetic field perpendicular to the (001) plane ($\theta = 90^\circ$), as shown in Figs. 7(a) and 7(b) for bulk single crystal and nanoflake device, respectively. The Hikami-Larkin-Nagaoka (HLN) formula

$$\Delta\sigma_{2D} = \left[-\frac{\alpha e^2}{2\pi^2\hbar}\right]\left[\ln\left(\frac{\hbar}{4eL_\varphi^2 B}\right) - \Psi\left(\frac{1}{2} + \frac{\hbar}{4eL_\varphi^2 B}\right)\right]$$

is used to fit the magnetoconductance observed in both bulk and nanoflake devices, where $\Delta\sigma_{2D}$ is the two-dimensional conductivity ($\Delta\sigma_{2D} = \frac{\Delta G \cdot L}{W}$, L and W are the length and width of transport channel, respectively), Ψ is the digamma function, L_φ is the phase coherence length, and α is a prefactor, which contains information about the nature of the electrons in topological insulators.[42,46] The fitted curves are plotted in Figs. 7(a) and 7(b) in solid lines. Due to the three-dimensional bulk contribution, the fitting curves do not agree well with experimental data for bulk single crystal samples. For the nanoflake device, the two-dimensional fitting curves agree very well with the experimental data for both fitting range from 0 to 2 Tesla and from 0 to 0.5 Tesla at all temperatures from 2 K to 45 K. The fitting results of α and L_φ of nanoflake devices are shown in Figs. 7(c) and 7(d), respectively. It is clear that similar results are obtained from different fitting ranges. The power-law fit gives $L_\varphi \propto T^{-0.66}$and $L_\varphi \propto T^{-0.19}$ (for the fitting of 0–0.5 Tesla field range) in the temperature regime 10 K–45 K and 2 K–7 K, respectively, which indicates the effect of phonon scattering at high temperatures and paramagnetic impurities at low temperatures.[44,45] It should be noted that the fitted L_φ at all temperatures are much smaller than the thickness of the sample (596 nm), which strongly indicates that the two-dimensional electron transport characteristics are due to the surface states. From this point of view, our experiment is very different from previous measurements on ultrathin Bi_2Se_3 and Bi_2Te_3 films. The two-dimensional transport behavior in ultrathin Bi_2Se_3 and Bi_2Te_3 films cannot be completely attributed to the surface states, because theL_φ is larger than the thickness of the film and therefore the film itself, including the bulk and surface states, forms a two-dimensional transport system. Since the thickness (596 nm) of our nanoflake BSTS device is much larger than L_φ(∼180 nm at 2 K, ∼110 nm at 10 K, and ∼60 nm at 30 K), it is a three-dimensional transport system. The two-dimensional

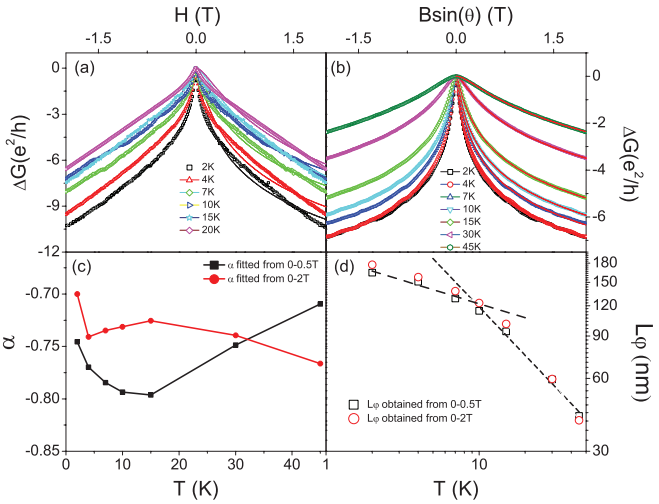

FIG. 7. (Color online) Temperature-dependent magnetoconductance of the BSTS single crystal and 596-nm thick nanoflake device with $\theta = 90^\circ$. (a) Magnetoconductance of the bulk single crystal at different temperatures. The HNL fitting curves are plotted in solid lines. (b) Magnetoconductance of the nanoflake device at different temperatures. The HNL fitting curves are plotted in solid lines. (c) The fitted values of α at different temperatures for the nanoflake device in the fitting range of 0–2 Tesla and 0–0.5 Tesla, respectively. (d) The power-law fit gives $L_\varphi \propto T^{-0.66}$and $L_\varphi \propto T^{-0.19}$ (0.5 Tesla) in the temperature regime 10–45 K and 2–7 K, respectively,

transport behavior of weak antilocalization can only originate from the helical surface states. The coefficient α takes a value of $-1/2$ for a traditional 2D electron system with strong spin-orbit coupling and one helical surface with a single Dirac cone. Since carriers on both the top and bottom surface can contribute the conduction in topological insulator samples, the ideal value of α is -1. As shown in Fig. 7(c), the perfect fitting using HLN formula generates α values between -0.7 to -0.8 at various temperatures, which also agrees with the 2D surface transport.

V. TIME-DEPENDENT UNIVERSAL CONDUCTANCE FLUCTUATION

We also observed a conductance fluctuation phenomenon in the nanoflake device under both low and high magnetic fields. The low magnetic field conductance fluctuation is very clear as shown in Figs. 6(b) and 6(f). Figure 8(a) shows the conductance fluctuations at different temperatures below 10 K and between 4 and 9 Tesla perpendicular fields. Different from normal universal conductance fluctuations (UCF) discovered in topological insulator Bi_2Se_3,[22,31] the conductance fluctuation in our nanoflake device evolves with time. Such a time-dependent UCF can only be observed below 10 K and the magnitude of those fluctuations increases with decreasing temperature. The top three curves shown in Fig. 8(a) were measured continuously with different field sweeping direction. As shown in the circled region in the figure, the curves show very similar fluctuation behaviors in the same magnetic field region because the time interval between the measurements is short. With the time evolution, the fluctuation patterns become

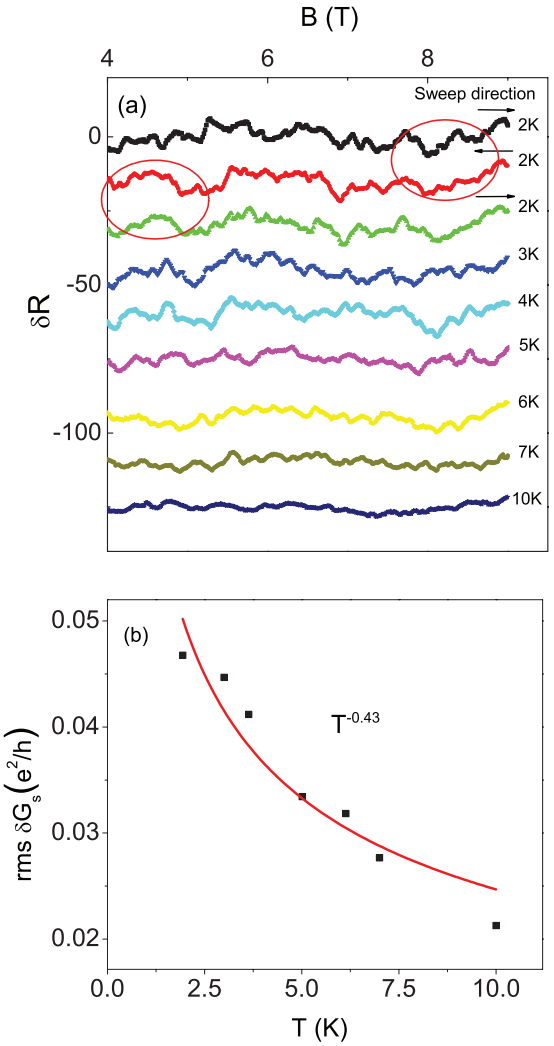

FIG. 8. (Color online) (a) Magnetofingerprint (UCF) signal δR vs magnetic field for the nanoflake device. At 2 K, we scan the field for three times with alternative field sweeping direction (the arrows). Seven UCF curves measured at temperatures between 2 K to 10 K were shown in the figures. (b) Temperature dependence of root mean square of the fluctuation of conductance. The solid line is the fitting curve using power law and the fitted power is -0.43.

different in the same magnetic field region. Time-dependent UCF is due to the sensitivity of the conductance to the motion of individual scatters and such phenomena have been reported. The variation of the conductance pattern is due to the motion of scattering sites, which changes the interference pattern of all the intersecting electronic paths in the coherent volume of the scattering sites. Since the motion of scattering sites is related to the time, the observed fluctuations are also time dependent, which allows the nonretraceable results. As the electron transport in the nanoflake is almost fully surface transport as discussed before, the motion of the scattering site might be due to the time-dependent surface contamination in the measurement chamber. Each magnetoresistance curve from 4–9 Tesla takes about one hour. According to the results, we can conclude that the scattering site pattern on the topological surface changes after about 30 minutes.

The amplitude of fluctuation detected is around $0.2e^2/h$. The phase coherence length of electron L_φ observed at 2 K is $\sim 0.18\ \mu$m (Fig. 7) and the thermal length, $L_T = \sqrt{hD/k_BT}$ is around 1μm at 2 K. As $L_\varphi < L_T < L$, the fluctuation of G can be calculated as $\delta G = e^2/h[L_\varphi/L]^{4-d}$, where L is the sample size. The calculated δG is $0.3e^2/h$, which is quite close to our experiment data $0.2e^2/h$ at 2 K. Furthermore, the root-mean-square (rms) of δG vs temperature curve is also plotted as shown in Fig. 8(b). The rms of δG is usually following the power law $rms\delta G \propto T^{-0.5}$ for a two-dimensional system. Our fitting shows $rms\delta G \propto T^{-0.43}$, which also indicates that the time-dependent UCF observed in the BSTS device sample is mainly from the surface states.

VI. CONCLUSION

In conclusion, we demonstrate surface-dominated transport in single crystalline nanoflake devices of topological insulator BSTS. The analysis on the resistivity and Hall resistance based on a two-channel model indicates that ~99% of the surface transport contribution can be realized in 200-nm thick BSTS devices. The pronounced electric gated ambipolar behavior of BSTS devices with a thickness of several hundred nanometers proves the dominated topological surface transport. Moreover, the angle-dependent weak antilocalization effect of bulk single crystals and nanoflake devices strongly suggest the surface-dominated transport in a nanoflake device, which is further confirmed by the fact that the phase coherence length L_φ obtained by 2D HNL fitting is much smaller than the thickness of device.

ACKNOWLEDGMENTS

Support for this work came from Singapore National Research Foundation (RCA-08/018), MOE Tier 2 (MOE2010-T2-2-059) and the Research Grant Council of Hong Kong under Grant No. HKU705110P.

APPENDIX

Two-channel model for calculating Hall effect:
We use the Drude model

$$m\frac{d\vec{\upsilon}}{dt} = -e(\vec{E} + [\vec{\upsilon} \times \vec{B}]) - \frac{m\vec{\upsilon}}{\tau}, \tag{A1}$$

$$\vec{j} = ne\vec{\upsilon}. \tag{A2}$$

At steady state

$$e\vec{E} = -e[\vec{\upsilon} \times \vec{B}]) - \frac{m\vec{\upsilon}}{\tau}, \tag{A3}$$

$$\vec{E} = -\frac{1}{ne}[ne\vec{\upsilon} \times \vec{B}]) - ne\vec{\upsilon} \cdot \frac{m}{ne^2\tau}. \tag{A4}$$

Define

$$R_H = \frac{1}{ne}, \quad \text{and} \quad \rho = \frac{m}{ne^2\tau}. \tag{A5}$$

We obtain

$$\vec{E} = \rho \cdot \vec{j} - R_H(\vec{j} \times \vec{B}). \tag{A6}$$

When the magnetic field $\vec{B}$ points to the z direction, we obtain

$$\begin{pmatrix} E_x \\ E_y \end{pmatrix} = \begin{pmatrix} \rho - R_H H \\ R_H H\rho \end{pmatrix} \begin{pmatrix} j_x \\ j_y \end{pmatrix}. \tag{A7}$$

Then the conductivity

$$\hat{\sigma} = \begin{pmatrix} \rho - R_H H \\ R_H H\rho \end{pmatrix}^{-1} = \frac{1}{\rho^2 + (R_H H)^2} \begin{pmatrix} \rho R_H H \\ -R_H H\rho \end{pmatrix}. \tag{A8}$$

For more than one channel transport,

$$\vec{j} = \sum_i \hat{\sigma}_i \vec{E}. \tag{A9}$$

Using

$$\frac{1}{\rho} = ne\mu \quad \text{and} \quad \frac{R_H}{\rho} = \mu, \tag{A10}$$

we obtain

$$\sigma = \begin{pmatrix} \sum_i \frac{ne\mu_i}{1+\mu_i^2 B_i^2} & \sum_i \frac{ne\mu_i^2}{1+\mu_i^2 B_i^2} \\ \sum_i \frac{ne\mu_i^2 B}{1+\mu_i^2 B^2} & \sum_i \frac{ne\mu_i^2}{1+\mu_i^2 B^2} \end{pmatrix}. \tag{A11}$$

Using

$$\hat{\rho} = \hat{\sigma}^{-1}, \tag{A12}$$

for a two-channel system, we obtain

$$\rho_{xy}(B) = -\frac{B}{e}\frac{\left(n_1\mu_1^2 + n_2\mu_2^2\right) + B^2\mu_1^2\mu_2^2(n_1+n_2)}{(n_1\mu_1 + n_2\mu_2)^2 + B^2\mu_1^2\mu_2^2(n_1+n_2)^2}. \tag{A13}$$

The formula is for two three-dimensional transport channels. If channel 2 is a two-dimensional transport channel (thickness = 0), the formula should be written as

$$\rho_{xy}(B) = -\frac{B}{e}\frac{\left(n_b\mu_b^2 + n_s\mu_s^2/t\right) + B^2\mu_b^2\mu_s^2(n_b + n_s/t)}{(n_b\mu_b + n_s\mu_s/t)^2 + B^2\mu_b^2\mu_b^2(n_b + n_s/t)^2}, \tag{A14}$$

which is Eq. (3) in the main text. Here, t is the sample thickness.

Equation (A14) is clear for understanding physics concept. However, n_b, n_s, μ_b, and μ_s are very large numbers. It is difficult to use Eq. (A14) for curve fitting. By using Eq. (A10) or derive from Eq. (A8) directly, we transfer Eq. (A14) to another equation,

$$\rho_{xy}(B) = -\frac{\left(R_b\rho_s^2 + R_s\rho_b^2\right) + B^2R_b^2R_s^2(R_b + R_s)}{(\rho_b + \rho_s)^2 + B^2(R_b + R_s)^2}. \tag{A15}$$

Here, R_b and ρ_b are the Hall coefficient and resistivity of the bulk electrons. $R_s = t/en_s$ and $\rho_s = \rho_{\text{sheet}}/t$, where ρ_{sheet} is the surface sheet resistance.

It should be noted that the Hall fitting has some arbitrariness due to the multiple fitting parameters and the symmetric form of Eq. (A15). The fitting results can only be used as a kind of support to the results obtained from the fitting-based Eq. (2) [Figs. 2(c) and 2(d)].

*These two authors contributed equally to this paper.
†wanglan@ntu.edu.sg

[1]L. Fu, C. L. Kane, and E. J. Mele, Phys. Rev. Lett. **98**, 106803 (2007).
[2]J. E. Moore, Nature (London) **464**, 194 (2010).
[3]X. L. Qi and S. C. Zhang, Phys. Today **63**, 33 (2010).
[4]M. Z. Hasan and C. L. Kane, Rev. Mod. Phys. **82**, 3045 (2010).
[5]Y. Xia, D. Dian, D. Hsieh, L. Wray, A. Pal, H. Lin, A. Bansil, D. Grauer, Y. S. Hor, R. J. Cava, and M. Z. Hasan, Nature Phys. **5**, 398 (2009).
[6]Y. L. Chen, J. G. Analytis, J. H. Chu, Z. K. Liu, S. K. Mo, X. L. Qi, H. J. Zhang, D. H. Lu, X. Dai, Z. Fang, S. C. Zhang, I. R. Fisher, Z. Hussain, and Z. X. Shen, Science **325**, 178 (2009).
[7]D. Hsieh, Y. Xia, L. Wray, D. Qian, A. Pal, J. H. Dil, J. Osterwalder, F. Meier, G. Bihlmayer, C. L. Kane, Y. S. Hor, R. J. Cava, and M. Z. Hasan, Science **323**, 919 (2009).
[8]T. Hirahara, Y. Sakamoto, Y. Takeichi, H. Miyazaki, S. I. Kimura, I. Matsuda, A. Kakizaki, and S. Hasegawa, Phys. Rev. B **82**, 155309 (2010).
[9]C. Jozwiak, Y. L. Chen, A. V. Fedorov, J. G. Analytis, C. R. Rotundu, A. K. Schmid, J. D. Denlinger, Y. D. Chuang, D. H. Lee, I. R. Fisher, R. J. Birgeneau, Z. X. Shen, Z. Hussain, and A. Lanzara, Phys. Rev. B **84**, 165113 (2011).
[10]D. Hsieh, Y. Xia, D. Qian, L. Wray, J. H. Dil, F. Meier, J. Osterwalder, L. Patthey, J. G. Checkelsky, N. P. Ong, A. V. Fedorov, H. Lin, A. Bansil, D. Grauer, Y. S. Hor, R. J. Cava, and M. Z. Hasan, Nature (London) **460**, 1101 (2009).
[11]K. Miyamoto, A. Kimura, T. Okuda, H. Miyahara, K. Kuroda, H. Namatame, M. Taniguchi, S. V. Eremeev, T. V. Menshchikova, E. V. Chulkov, K. A. Kokh, and O. E. Tereshchenko, Phys. Rev. Lett. **109**, 166802 (2012).
[12]S. Souma, K. Kosaka, T. Sato, M. Komatsu, A. Takayama, T. Takahashi, M. Kriener, K. Segawa, and Y. Ando, Phys. Rev. Lett. **106**, 216803 (2011).
[13]S. Y. Xu, L. A. Wray, Y. Xia, F. von Rohr, Y. S. Hor, J. H. Dil, F. Meier, B. Slomski, J. Osterwalder, M. Neupane, H. Lin, A. Bansil, A. Fedorov, R. J. Cava, and M. Z. Hasan, arXiv:1101.3985.
[14]Z. Alpichshev, J. G. Analytis, J. H. Chu, I. R. Fisher, Y. L. Chen, Z. X. Shen, A. Fang, and A. Kapitulnik, Phys. Rev. Lett. **104**, 016401 (2010).
[15]T. Zhang, P. Cheng, X. Chen, J.-F. Jia, X. C. Ma, K. He, L. L. Wang, H. J. Zhang, X. Dai, Z. Fang, X. C. Xie, and Q. K. Xue, Phys. Rev. Lett. **103**, 266803 (2009).
[16]L. Fu and C. L. Kane, Phy. Rev. Lett. **100**, 096407 (2008).
[17]X. L. Qi, R. Li, J. Zang, and S. C. Zhang, Science **323**, 1184 (2009).
[18]R. Yu, W. Zhang, H. J. Zhang, S. C. Zhang, X. Dai, and Z. Fang, Science **329**, 61 (2010).
[19]J. G. Analytis, J. H. Chu, Y. Chen, F. Corredor, R. D. McDonald, Z. X. Shen, and I. R. Fisher, Phys. Rev. B **81**, 205407 (2010).
[20]Y. S. Hor, A. Richardella, P. Roushan, Y. Xia, J. G. Checkelsky, A. Yazdani, M. Z. Hasan, N. P. Ong, and R. J. Cava, Phys. Rev. B **79**, 195208 (2009).
[21]J. G. Checkelsky, Y. S. Hor, R. J. Cava, and N. P. Ong, Phys. Rev. Lett. **106**, 196801(2011).
[22]J. G. Checkelsky, Y. S. Hor, M.-H. Liu, D.-X. Qu, R. J. Cava, and N. P. Ong, Phys. Rev. Lett. **103** 246601 (2009).
[23]N. P. Butch, K. Kirshenbaum, P. Syers, A. B. Sushkov, G. S. Jenkins, H. D. Drew, and J. Paglione, Phys. Rev. B **81**, 241301 (2010).
[24]D. X. Qu, Y. S. Hor, J. Xiong, R. J. Cava, and N. P. Ong, Science **329**, 821 (2010).
[25]H. Peng, K. Lai, D. Kong, S. Meister, Y. Chen, X.-L. Qi, S.-C. Zhang, Z.-X. Shen, and Y. Cui, Nat. Mater. **9**, 225 (2010).
[26]J. Chen, H. J. Qin, F. Yang, J. Liu, T. Guan, F. M. Qu, G. H. Zhang, J. R. Shi, X. C. Xie, C. L. Yang, K. H. Wu, Y. Q. Li, and L. Lu, Phys. Rev. Lett. **105**, 176602 (2010).
[27]Y. S. Kim, M. Brahlek, N. Bansal, E. Edrey, G. A. Kapilevich, K. Iida, M. Tanimura, Y. Horibe, S. W. Cheong, and S. Oh, Phys. Rev. B **84**, 073109 (2011).
[28]M. Liu, J. Zhang, C. Z. Chang, Z. Zhang, X. Feng, K. Li, K. He, L. L. Wang, X. Chen, X. Dai, Z. Fang, Q. K. Xue, X. Ma, and Y. Wang, Phys. Rev. Lett. **108**, 036805 (2012).
[29]M. Liu, C. Z. Chang, Z. Zhang, Y. Zhang, W. Ruan, K. He, L. L. Wang, X. Chen, J. F. Jia, S. C. Zhang, Q. K. Xue, X. Ma, and Y. Wang, Phys. Rev. B **83**, 165440 (2011).
[30]H. T. He, G. Wang, T. Zhang, I. K. Sou, G. K. L. Wong, J. N. Wang, H. Z. Lu, S. Q. Shen, and F. C. Zhang, Phys. Rev. Lett. **106**, 166805 (2011).
[31]S. Matsuo, T. Koyama, K. Shimamura, T. Arakawa, Y. Nishihara, D. Chiba, K. Kobayashi, T. Ono, C. Z. Chang, K. He, X. C. Ma, and Q. K. Xue, Phys. Rev. B **85**, 075440 (2012).
[32]H. Steinberg, D. R. Gardner, Y. S. Lee and P. Jarillo-Herrero, Nano Lett. **10**, 5032 (2010).
[33]Z. Ren, A. A. Taskin, S. Sasaki, K. Segawa, and Y. Ando, Phys. Rev. B **82**, 241306 (2010).
[34]S. Jia, H. Ji, E. Climent-Pascual, M. K. Fuccillo, M. E. Charles, J. Xiong, N. P. Ong, and R. J. Cava, Phys. Rev. B **84**, 235206 (2011).
[35]J. Xiong, A. C. Petersen, D. Qu, R. J. Cava, and N. P. Ong, Physica E **44**, 917 (2012).
[36]T. Arakane, T. Sato, S. Souma, K. Kosaka, K. Nakayama, M. Komatsu, T. Takahashi, Z. Ren, K. Segawa, and Y. Ando, Nature Commun. **3**, 636 (2012).
[37]A. A. Taskin, Z. Ren, S. Sasaki, K. Segawa, and Y. Ando, Phys. Rev. Lett. **107**, 016801 (2011).
[38]Z. Ren, A. A. Taskin, S. Sasaki, K. Segawa, and Y. Ando, Phys. Rev. B **84** 075316 (2011).
[39]S. S. Hong, J. J. Chua, D. S. Kong, and Y. Cui, Nature Commun. **3**, 757 (2012)
[40]D. Kim, S. Cho, N. P. Butch, P. Syers, K. Kirshenbaum, S. Adam, J. Paglione and M. S. Fuhrer, Nature Phys. **8**, 459 (2012).
[41]K. S. Novoselov, A. K. Geim, S. V. Morozov, D. Jiang, Y. Zhang, S. V. Dubonos, I. V. Grigorieva, A. A. Firsov, Science **306**, 666 (2004)
[42]H. Z. Lu, and S. Q. Shen, Phys. Rev. B **84**, 125138 (2011).
[43]J. Wang, A. M. DaSilva, C. Z. Chang, K. He, J. K. Jain, N. Samarth, X. C. Ma, Q. K. Xue, and M. H. W. Chan, Phys. Rev B **83**, 245438 (2011).
[44]E. McCann, K. Kechedzhi, V. I. Fal'ko, H. Suzuura, T. Ando, and B. L. Altshuler, Phys. Rev. Lett. **97**, 146805 (2006).
[45]G. Bergmann, Phys. Rep. **107**, 1 (1984).
[46]B. L. Altshuler, A. G. Aronov and D. E. Khmelnitsky, J. Phys. C: Solid State Phys. **15**, 7367 (1982).